Effects of elastic anisotropy on the flow and orientation of sheared nematic liquid crystals

Jianjun Tao[a] and James J. Feng[b]

The Levich Institute for Physicochemical Hydrodynamics, City College of City University of New York, New York, New York 10031

(Received 23 December 2002; final revision received 25 April 2003)

Synopsis

We use a finite-difference algorithm to simulate the shear flow of nematic liquid crystals based on the Leslie–Ericksen theory, and investigate how unequal elastic constants affect the formation, oscillation, and breakup of roll cells, the nucleation of defects, and the coarsening of texture upon cessation of flow. With elastic anisotropy, the so-called Ericksen number (Er) cascade comprises the same regimes previously documented for isotropic elasticity: stable simple shear, steady roll cells, oscillatory roll cells, and an irregular pattern with thick disclinations. The onset of roll cells is most sensitive to K_3, the elastic constant for bend. Increasing K_3 stabilizes the shear flow against the formation of rolls. For reduced K_3, a second Er cascade may appear for higher Er, with regularization and eventual reappearance of the defect-laden irregular pattern. The twist constant K_2 is the most important for defect formation; a weaker K_2 causes roll cells to breakup and pairs of ± 1 defects to nucleate at lower Er. The defects show distinctive structures depending on the elastic anisotropy; typically a weaker elastic constant gives rise to patterns that incur greater distortion in the corresponding mode. After cessation of shear, all textures relax completely to a monodomain. The longest-lasting orientational pattern is again attributable to the weakest of the elastic constants. By analyzing the amount of distortion in each mode and the associated free energy, we are able to elucidate the role of elastic anisotropy in defining the orientational patterns in sheared nematics.
 [DOI: 10.1122/1.1584429]

I. INTRODUCTION

Texture and defects are perhaps the most characteristic attributes of liquid crystals (LCs) and liquid-crystalline polymers (LCPs), and the birth of defects in a flowing and initially defect-free liquid-crystalline material has been an issue of long-standing interest [Larsen (1993); Rey and Denn (2002)]. Shearing small-molecule nematic LCs, Mather (1996a, 1996b) discovered that disclination lines nucleate in the bulk only for tumbling liquid crystals. In flow-aligning liquid crystals, defects originate on solid boundaries and in much smaller numbers. These findings have confirmed the long-held view that director tumbling is fundamentally responsible for the defects in liquid-crystalline materials. Larson and Mead (1992; 1993) published a series of experiments on slow shearing flows of poly(benzylglutamate) (PBG) solutions, which is a tumbling LCP [Burghardt and Fuller (1990)]. The director **n** is initially aligned with the vorticity direction. With increasing shear rate (or Ericksen number Er), the texture of the sample changed from that of a monodomain to regular parallel stripes, then to irregular stripes with thick disclinations

[a]Present address: LIMSI-CNRS, BP133, 91403 Orsay Cedex, France.
[b]Author to whom all correspondence should be addressed; electronic mail: feng@ccny.cuny.edu

parallel to the flow, and finally to a chaotic pattern. This series of changes in the birefringent pattern, apparently rooted in distortional elasticity, is known as the Ericksen number cascade.

Linear instability analyses indicate that the regular stripes are due to rolls of counter-rotating cells oriented along the flow [Manneville and Dubois-Violette (1976); Larson (1993)], and the experiments of Larson and Mead (1993) strongly suggest that roll cells play a key role in the formation of disclinations. However, details of the process are inaccessible to linear instability analysis, and experimental observations at sufficient resolutions would be difficult as well. This motivated Feng *et al.* (2001) to perform dynamic simulations of sheared nematics using the Leslie–Ericksen (LE) theory. Numerical results reveal four flow regimes with increasing Er: stable simple shear, steady roll cells, oscillating roll cells, and irregular patterns with disclinations. These are in general agreement with Larson and Mead's (1992; 1993) experiments on PBG solutions. In particular, the simulations identified a route for the nucleation of thick disclinations in sheared nematics. In the last regime, roll cells break up to form ''ridges'', elongated regions where the director is swept into the flow direction. Given favorable local flow conditions, a ridge splits to produce a pair of ± 1 disclinations of the escaped type with nonsingular cores. These disclinations are parallel to the flow and persist for some time before annihilating between pairs of opposite signs.

A caveat is that these simulations have assumed elastic isotropy. Within the framework of Frank elasticity, distortions of the director field $\mathbf{n}(\mathbf{r})$ can be classified into the three canonical modes: splay, twist and bend [de Gennes and Prost (1993)]. The total free energy may be written as the sum of contributions from each mode

$$F = \frac{K_1}{2}(\nabla\cdot\mathbf{n})^2 + \frac{K_2}{2}[\mathbf{n}\cdot(\nabla\times\mathbf{n})]^2 + \frac{K_3}{2}|\mathbf{n}\times(\nabla\times\mathbf{n})|^2, \tag{1}$$

where the coefficients K_1, K_2, and K_3 are Frank elastic constants representing splay, twist, and bend, respectively. Elastic isotropy is the assumption that all three constants are equal, also known as the one-constant assumption. This brings about algebraic simplifications in the theory [de Gennes and Prost (1993)]. For instance, the free energy of Eq. (1) reduces to

$$F = \frac{K}{2}\nabla\mathbf{n}:(\nabla\mathbf{n})^T, \tag{2}$$

where K is the single elastic constant. However, real nematic fluids have disparate elastic constants, a quality referred to as elastic anisotropy. For small-molecule LCs, typically, twist is the lowest energy mode while bend and splay are on a par. For polymeric liquid crystals, splay tends to be the costliest mode and more importantly, the degree of anisotropy is much greater than for small-molecule LCs. Tabulated values for a number of materials in both categories may be found in Larson (1993).

Apparently, the assumption of elastic isotropy is unrealistic. Furthermore, experimental evidence indicates a prominent role for elastic anisotropy in determining the conformation of orientational defects [Hudson and Thomas (1989); Hudson *et al.* (1993); Wang *et al.* (1994)]. Previous studies of elastic anisotropy, as far as we know, concern static defects of $\pm 1/2$ strength within a two-dimensional director field. As such, the twist mode is excluded, as are any dynamics that may manifest themselves during flow. Theoretically, Larson (1993) studied the linear instability of shear flow between parallel plates, and computed the neutral curves for several elastically anisotropic nematics. He found that K_2 has little effect on the critical Er for the onset of roll-cell instability. This

surprising result, though limited to infinitesimal distortions, gives a glimpse into the intriguing roles that elastic anisotropy may play in general flow situations with more severe distortions. To date, there has not been a systematic study of elastic anisotropy in flowing LCs or LCPs, especially regarding the nucleation and conformation of flow-induced disclinations.

This lack of knowledge serves as the rationale for the study reported here. By generalizing the prior work of Feng *et al.* (2001), we numerically simulate the shear flow of nematics with unequal elastic constants. By examining the Ericksen cascade, we elucidate the roles of elastic anisotropy in a series of dynamic phenomena, from the onset of roll cells to their eventual breakup, and to coarsening upon cessation of flow, with an emphasis on the occurrence and structure of defects.

In the context of prior experimental and theoretical studies of LCs and LCPs, we should emphasize two points relevant to the significance of this work. First, the simulations concern an idealized system. The mathematical model and flow geometry are such as to contain the essential characteristics of the problem while keeping it simple enough for detailed numerical analysis. The material parameters are chosen largely to map out the model behaviors of interest rather than to approximate a particular nematic. These should be borne in mind when correlating the numerical results to experimental observations. Second, the Leslie–Ericksen theory to be used here constitutes an asymptotic limit, for small distortions and weak flows, of several LCP constitutive theories. For instance, it may be seen as the result of coarse-graining molecularly-based or phenomenological tensor theories [Rey and Tsuji (1998); Feng *et al.* (2000); Kupferman *et al.* (2000); Wang (2002)]. These, in turn, are coarse-grain approximations of kinetic theories [Suen *et al.* (2002)]. Thus, this paper represents initial steps toward multiscale simulation of flowing LCPs, and the results should serve as guidelines for future studies with more sophisticated models.

II. FORMULATION OF THE PROBLEM

Our simulations are based on the LE theory. There are several reasons for this choice. The first is the simplicity of the LE theory in comparison with molecular theories [e.g., Feng *et al.* (2000)]. The molecular configuration is only represented by the direction **n**, the orientation distribution being assumed fixed at the equilibrium state. The second is the theory's capability to describe the weak flows and mild spatial distortions in the Ericksen number cascade. Molecular viscoelasticity, absent from the LE theory, becomes dominant only in the Deborah number cascade for LCPs [Larson and Mead (1993)]. Thus, Feng *et al.* (2001) were able to reproduce, qualitatively at least, the flow instability and thick disclinations that Larson and Mead (1993) have observed in sheared PBG solutions. In fact, experiments show small-molecule LCs to behave similarly to LCPs in the Ericksen cascade [Mather *et al.* (1996b)]. Recently, Sgalari *et al.* (2002) explored the Deborah number cascade using the molecular theory of Feng *et al.* (2000). Though the molecular order parameter does vary appreciably, the qualitative behavior of in-plane tumbling and out-of-plane tipping are the same as predicted by the LE theory. Based on these, we expect our results to be relevant to the flow of small-molecule LCs and LCPs subject to weak flows and mild distortions. Finally, the LE theory is the common limit of more sophisticated models, and has been successfully used in numerous flow simulations, e.g., Han and Rey (1994; 1995), though their focus was not on roll-cell instability and defect formation.

The LE theory consists of two major equations [de Gennes and Prost (1993)]:

$$\mathbf{n}\times(\mathbf{h}-\gamma_1\mathbf{N}-\gamma_2\mathbf{n}\cdot\mathbf{D}) = 0, \tag{3}$$

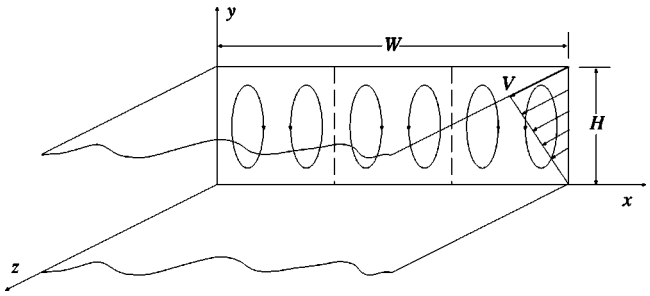

FIG. 1. Schematic of the computational domain. The top plane moves with velocity V while the bottom is fixed.

$$\boldsymbol{\sigma} = \boldsymbol{\sigma}^e + \alpha_1 \mathbf{D}:\mathbf{nnnn} + \alpha_2 \mathbf{nN} + \alpha_3 \mathbf{Nn} + \alpha_4 \mathbf{D} + \alpha_5 \mathbf{nn}\cdot\mathbf{D} + \alpha_6 \mathbf{D}\cdot\mathbf{nn}. \tag{4}$$

Equation (3) determines the rotation of the director $\mathbf{n}$ through the balance between an elastic torque and a viscous torque. The molecular field vector $\mathbf{h}$ is defined as the energy penalty for rotating $\mathbf{n}$:

$$\mathbf{h} = -\frac{\partial F}{\partial \mathbf{n}} + \nabla \cdot \frac{\partial F}{\partial(\nabla \mathbf{n})} \tag{5}$$

and has the physical meaning of an elastic torque on the director. $\mathbf{N} = \dot{\mathbf{n}} - \boldsymbol{\Omega}\cdot\mathbf{n}$ is the rotation of the director with respect to the background fluid, with $\boldsymbol{\Omega} = [(\nabla \mathbf{v})^T - \nabla \mathbf{v}]/2$ being the vorticity tensor and $\mathbf{v}$ being the velocity. $\mathbf{D} = [(\nabla \mathbf{v})^T + \nabla \mathbf{v}]/2$ is the strain rate tensor and γ_1 and γ_2 are viscosity constants. Equation (4) gives the stress tensor of the material, where $\boldsymbol{\sigma}^e$ is the Ericksen stress

$$\boldsymbol{\sigma}^e = -\frac{\partial F}{\partial(\nabla \mathbf{n})} \cdot (\nabla \mathbf{n})^T. \tag{6}$$

The α's are Leslie coefficients related to the γ's via

$$\gamma_1 = \alpha_3 - \alpha_2, \tag{7}$$

$$\gamma_2 = \alpha_3 + \alpha_2 = \alpha_6 - \alpha_5. \tag{8}$$

We consider the shear flow between two parallel planes separated by distance H, the bottom plane being stationary and the top moving with velocity V (Fig. 1). To make the equations dimensionless, we take V to be the characteristic velocity, H to be the characteristic length, and H/V to be the characteristic time. We also define $\eta = \alpha_4/2$ as the characteristic viscosity and use some K as the characteristic elastic constant. Inserting the free energy of Eq. (1) into Eqs. (5) and (6), and incorporating the stress tensor of Eq. (4) into the linear momentum equation, we arrive at the following dimensionless governing equations

$$\frac{\mathbf{n}}{\mathrm{Er}} \times \{K_3 \nabla^2 \mathbf{n} + (K_1 - K_3)\nabla(\nabla \cdot \mathbf{n}) + (K_3 - K_2)[Q\nabla \times \mathbf{n} + \nabla \times (Q\mathbf{n})]\}$$

$$= \mathbf{n} \times (\gamma_1 \mathbf{N} + \gamma_2 \mathbf{D}\cdot\mathbf{n}), \tag{9}$$

$$\nabla p - \nabla^2 \mathbf{v} = -\frac{\nabla \cdot \boldsymbol{\sigma}^e}{\mathrm{Er}} + \nabla \cdot (\alpha_1 \mathbf{D}:\mathbf{nnnn} + \alpha_2 \mathbf{nN} + \alpha_3 \mathbf{Nn} + \alpha_5 \mathbf{nn}\cdot\mathbf{D} + \alpha_6 \mathbf{D}\cdot\mathbf{nn}), \tag{10}$$

$$\nabla \cdot \mathbf{v} = 0, \tag{11}$$

where $Q = \mathbf{n}\cdot(\nabla \times \mathbf{n})$ and the Ericksen number is defined as

$$\mathrm{Er} = \frac{\eta V H}{K}. \tag{12}$$

For convenience, we use the same symbols for dimensionless quantities. Fluid inertia is neglected in comparison with the viscous stress since the flow varies on a time scale associated with the director rotation, which is much longer than that for viscous dissipation.

In the above, all viscosities have been scaled by η and all elastic constants by K. In the simulations, we fix the viscosity ratios at values for Larson's (1993) ''typical nematic polymer'' having the following dimensional viscosities:

$$(\alpha_1,\alpha_2,\alpha_3,\alpha_4,\alpha_5,\alpha_6) = (-45.91,-69.2,3.13,3.36,60.15,-5.69) \ \text{poise}. \tag{13}$$

Note that $\alpha_3/\alpha_2 < 0$ indicates a tumbling nematic. The ratios of the elastic constants, on the other hand, will not approximate those of a real nematic but rather be varied systematically so as to map out the effects of elastic anisotropy. The choice of K will be specified when discussing the results in Sec. III.

The numerical aspects of the problem are similar to those of the simpler problem with equal K's, and we will mention only the key features and refer the reader to Feng *et al.* (2001) for details. The computational domain is a rectangle in the x–y plane (Fig. 1) with an aspect ratio $W/H = 8$. We assume no variation along the flow direction (z axis) for the velocity components (u,v,w) and the director orientation (n_x,n_y,n_z). The governing equations are discretized using finite difference on a uniform staggered grid, and numerically integrated using a multigrid method. Mesh refinement has been carried out to confirm convergence. The discretization of Eq. (9) is done in a local principal coordinate system so that the constraint $|\mathbf{n}| = 1$ is easily imposed. For the velocity $\mathbf{v}$, we use no-slip boundary conditions on the top and bottom plates and impermeable and zero-shear-stress conditions on the sidewalls. The director $\mathbf{n}$ is anchored on all boundaries along the velocity direction (x axis), which ensures that the first instability be the roll cells [Larson and Mead (1993)]. The initial condition is the simple shear flow of a single crystal, with a uniform director field $\mathbf{n} = (1,0,0)$. We then supply a spatially random disturbance of amplitude 10^{-4} to the $\mathbf{n}$ field and follow the subsequent evolution of the flow and director orientation.

As a measure of the relative importance of the three modes of distortion, we define a dimensionless average free energy for each mode

$$\text{For splay: } F_s = \frac{K_1}{2A}\int_A (\nabla \cdot \mathbf{n})^2 dA, \tag{14}$$

$$\text{For twist: } F_t = \frac{K_2}{2A}\int_A [\mathbf{n}\cdot(\nabla \times \mathbf{n})]^2 dA, \tag{15}$$

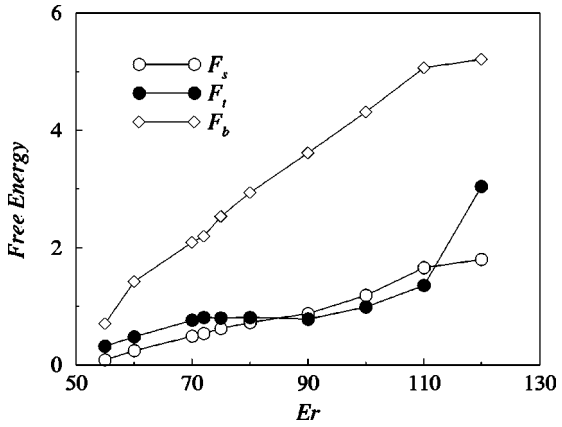

FIG. 2. Free energy for splay (F_s), twist (F_t), and bend (F_b) in the first three regimes of the Ericksen cascade for an elastically isotropic nematic.

$$\text{For bend: } F_b = \frac{K_3}{2A}\int_A |\mathbf{n}\times(\nabla\times\mathbf{n})|^2 dA, \tag{16}$$

where A is the area of our computational domain made dimensionless by H^2.

III. RESULTS AND DISCUSSIONS

The numerical results are discussed in five sections. In Sec. A, we analyze the three types of distortions for an elastically isotropic nematic. This serves as a base line for subsequent sections on elastic anisotropy. Section B focuses on how elastic anisotropy affects the onset of roll-cell instability. Section C examines the higher-Er regimes and constructs a complete picture on how elastic anisotropy modifies the Ericksen number cascade. Section D discusses the occurrence and structure of defects. Finally, Sec. E investigates the coarsening of texture and relaxation of distortions upon cessation of the shear.

A. Splay, twist, and bend in an elastically isotropic nematic

We wish to understand how each mode of distortion evolves in the elastically isotropic solutions of Feng *et al.* (2001). This special case then serves as a base line for analyzing more general cases. Feng *et al.* (2001) showed that with elastic isotropy, the Ericksen cascade consists of four regimes: simple shear of monodomain (Er $<$ 50), steady roll cells (50 $<$ Er $<$ 90), oscillatory roll cells (90 $<$ Er $<$ 120), and finally irregular pattern with defects (Er $>$ 120). By carrying out simulations at smaller intervals of Er, we have refined the critical Er values in this study so they differ somewhat from those given in Feng *et al.* (2001).

For the steady roll-cell regime, we can define a unique free energy for each mode according to Eqs. (14)–(16). Time averaging is used for the oscillating roll cells. Figure 2 plots the free energies for splay, twist, and bend at different Er covering the first three regimes. The most pronounced feature is that the bending energy F_b is by far the largest of the three. The dominance of the bending mode can be easily understood from the director field in Fig. 3. The roll-cell instability produces, inside each swirl, mostly rotation of **n** inside the plane of the secondary flow, i.e., the x–y plane. This gives rise to a strong bending component. The small tipping of **n** out of the x–y plane toward the flow

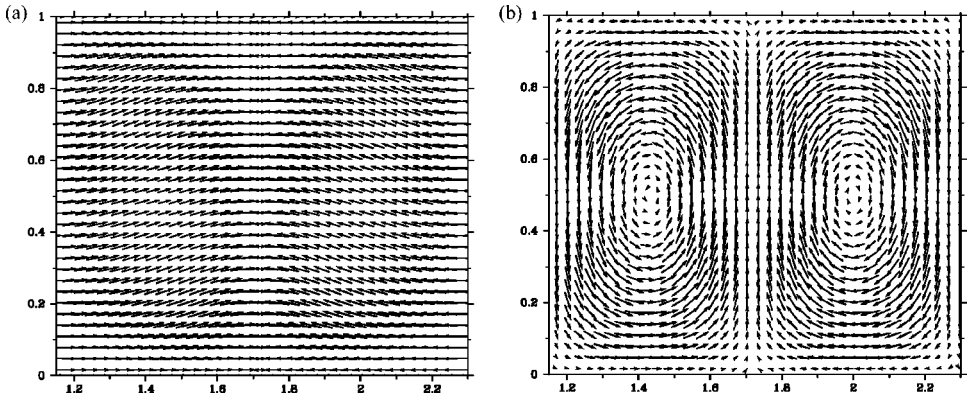

FIG. 3. A steady pair of roll cells for an elastically isotropic nematic at Er = 70. (a) The director field $\mathbf{n}(\mathbf{r})$, where tipping out of the plane is indicated by a shorter arrow; (b) the velocity vector (u,v) for the secondary flow in the $x-y$ plane. The maximum velocity is 1.44% of that of the top plane V.

direction is responsible for the smaller twist, while splay has the lowest energy for smaller Er. Another notable feature is that all three energies tend to increase with Er, indicating more severe distortions at higher shear rates. An exception is a tiny dip in the twist energy F_t near the onset of oscillatory cells (Er $\approx$ 90). Toward the upper end of the oscillatory regime, F_t shoots up sharply. This corresponds to the rotation of **n** into the flow direction in the core of the cells, a precursor to the formation of ridges.

The fourth regime (Er $>$ 120) features an interesting temporal evolution. From the initial monodomain, regular roll cells form quickly, and then start to split between the top and the bottom. The daughter cells undergo further breakup and coalescence as the spatial pattern becomes irregular. The core of some daughter cells become ridges where **n** is swept into the flow direction. Some of the ridges then split to produce pairs of escaped ± 1 disclinations. Details of the process are given in Feng *et al.* (2001). For our present purpose, Fig. 4(a) illustrates the temporal evolution at Er = 200 in terms of the three distortion energies. Regular roll cells emerge at $t \approx 10$ strain units and persist till $t \approx 40$. During this period, the distortion is predominantly bend as in the regime of steady roll cells. After the cells start to split, F_b and F_s peak at $t \approx 50$ as F_t shoots up sharply; the

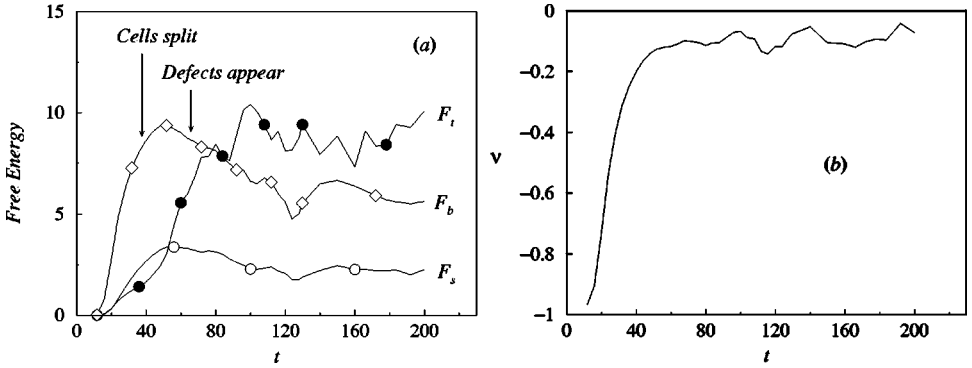

FIG. 4. (a) Temporal evolution of the free energies for an elastically isotropic nematic at Er = 200. The nonsmoothness of the data is an artifact due to our calculating the energies every 200–500 time steps; (b) evolution of the global alignment parameter ν.

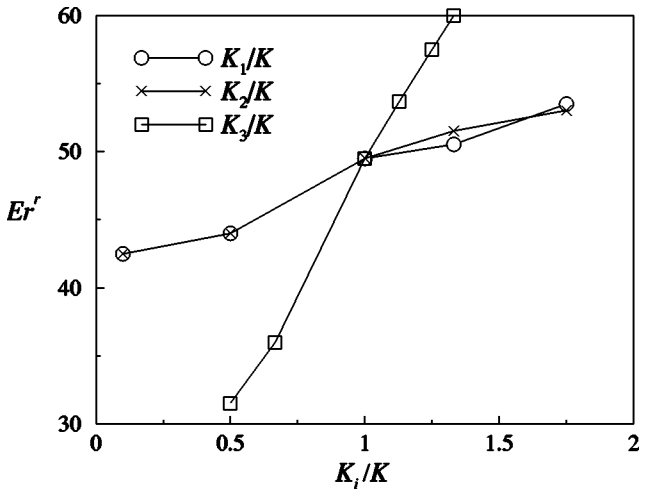

FIG. 5. Critical Er^r for the roll-cell instability as a function of elastic anisotropy. For each curve, one elastic constant is varied while the other two are kept equal and fixed.

scenario resembles the high-Er end of the oscillatory-cell regime in Fig. 2. Again, the pronounced twist corresponds to the rotation of **n** into the flow direction during the formation of ridges. After defects form at $t \approx 60$, the three modes settle into more or less steady values, with irregular fluctuations. In this ''quasisteady'' state, F_t remains the largest while F_s the smallest. Hence, the final regime is characterized by strong twist associated with ridges and escaped ± 1 defects.

Hongladarom *et al.* (1993) investigated the effect of shear on molecular orientation in PBG solutions by measuring the birefringence. Their data correspond, in our context, to a global measure of the director orientation: $\nu = \langle n_z^2 \rangle - \langle n_x^2 \rangle$, where the bracket represents averaging over the entire domain. They reported ν values ranging from 0.53 to 0.63 in the regime of director turbulence. In our simulation [Fig. 4(b)], ν starts from a value of -1, corresponding to the initial uniform orientation along the x axis, and climbs up almost in synchronization with the twist energy F_t. Eventually, ν fluctuates around a value of -0.05, which, though well below the measured values of Hongladarom *et al.* (1993), shows that the flow has come a long way in turning **n** against the wall anchoring.

To sum up, the analysis of elastically isotropic solutions suggests that of the three modes, bend or K_3 has the greatest effect on the onset and evolution of roll cells, whereas twist or K_2 dominates the final regime of irregular patterns with defects. The validity of these observations in solutions with anisotropic elasticity will be examined in the following.

B. Critical Er for the onset of roll-cell instability

To systematically explore the effects of elastic anisotropy, we keep two of the three elastic constants equal and fixed, and vary the third one alone. The fixed value is then taken to be the characteristic K based on which Er is defined. This protocol will be used for the rest of the paper, and this section is concerned with the critical condition for the onset of roll-cell instability.

The critical Ericksen number Er^r for the onset of roll cells is determined to within ± 0.5 from simulations for a range of Er. Figure 5 shows how Er^r varies with each of the three K's. The intersection of the three curves corresponds to the isotropic case. Increas-

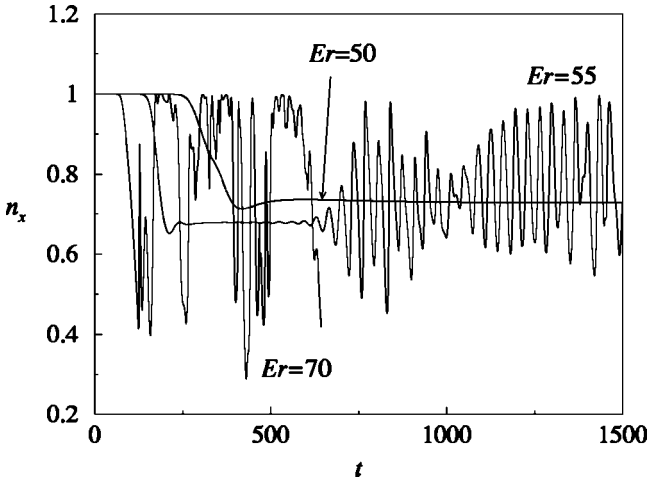

FIG. 6. Small K_1: evolution of the x component of the director at a fixed point (2,0.25) for Er = 50, 55, and 70.

ing any elastic constant, as one may expect, raises Er^r and stabilizes the flow against roll-cell instability. The effect is strongest for K_3 and much weaker for K_1 and K_2. This is consistent with the observations made of Fig. 3 that the onset of rolls involves mostly bend. The weak effect of K_2 has been noted previously by Larson (1993) from linear instability analysis. As a validation of our numerical code, we have also computed Er^r using additional sets of parameters given by Larson (1993) for 8CB and the ''typical nematic polymer.'' Good agreement is obtained for Er^r as well as the critical wave number q_x.

C. Anisotropic effects on the higher-Er regimes

When Er increases beyond Er^r, Feng *et al.* (2001) found three additional regimes in the special case of elastic isotropy: steady roll cells, oscillatory roll cells, and an irregular and fluctuating pattern with defects. To explore the effects of elastic anisotropy on the higher-Er regimes, we will examine three cases: $K_1 = 0.1K$, $K_2 = K_3 = K$ (small K_1); $K_2 = 0.1K$, $K_1 = K_3 = K$ (small K_2); $K_3 = 0.5K$, $K_1 = K_2 = K$ (small K_3).

Small K_1. To illustrate the temporal evolution of the solutions, Fig. 6 plots the history of the director component n_x along the vorticity direction at an arbitrarily chosen spatial point $(x,y) = (2,0.25)$. For different solutions, this point will be at different positions relative to, say, a nearby roll cell. Thus, the magnitude of n_x is not meaningful by itself. But the qualitative nature of its evolution reflects that of the entire solution. for Er between $\mathrm{Er}^r = 42.5$ and a threshold $\mathrm{Er}^o \approx 52$, steady roll cells prevail, and a solution at Er = 50 is shown as an example. With increasing Er, the secondary flow intensifies in terms of the magnitude of velocity components u and v. The dominant wave number q_x is also expected to increase with Er (Feng *et al.* 2001). Because of the specification that the side walls be cell boundaries, our geometry allows only discrete changes in the wave number. Thus, the change of q_x over this narrow range of Er is not reflected by our simulations; the number of cells remains at 14 across the channel width of $W = 8H$. As Er surpasses Er^o, the roll cells form and then start oscillating, in much the same way as for the previously studied isotropic case. The only difference is that the amplitude is modulated as illustrated by Er = 55 in Fig. 6. It is possible that constant-amplitude

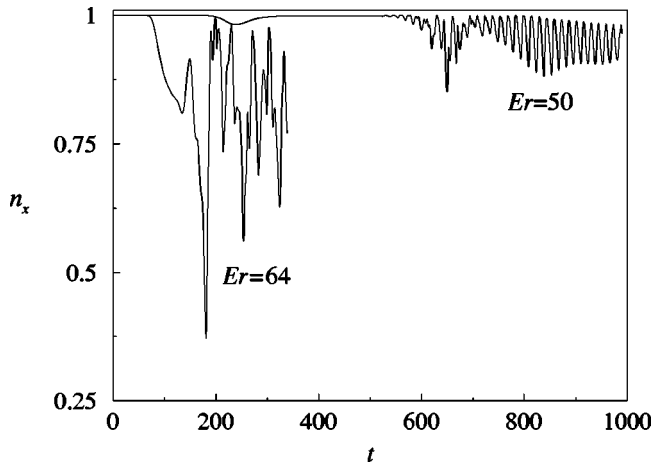

FIG. 7. Small K_2: evolution at n_x at $(x,y) = (2,0.25)$ for Er = 50 and 64.

oscillation exists just above Er^o. When Er exceeds still another threshold Er^i, estimated to be near 65, regular roll cells form first and then rapidly breakup into an irregular pattern that also fluctuates in time. Thick disclination lines nucleate, with ± 1 strength in the escaped configuration. This regime again resembles that for isotropy elasticity. The effects of unequal K's on the conformation of the defects will be investigated in Sec. D.

Small K_2. The regimes are qualitatively the same as for small K_1, with transitions from steady rolls to oscillating rolls at $\mathrm{Er}^o \approx 47$, and further to irregular patterns with defects at $\mathrm{Er}^i \approx 57$. Again, we have only obtained amplitude-modulated oscillations in the intermediate regime, though we cannot rule out the possibility of a narrow Er range just above Er^o where the oscillation has a constant amplitude. Examples of the last two regimes are shown in Fig. 7.

Small K_3. With increasing Er, we initially see the same transitions as earlier, with $\mathrm{Er}^o \approx 55$ and $\mathrm{Er}^i \approx 62.5$. If we continue to increase the Ericksen number, however, the

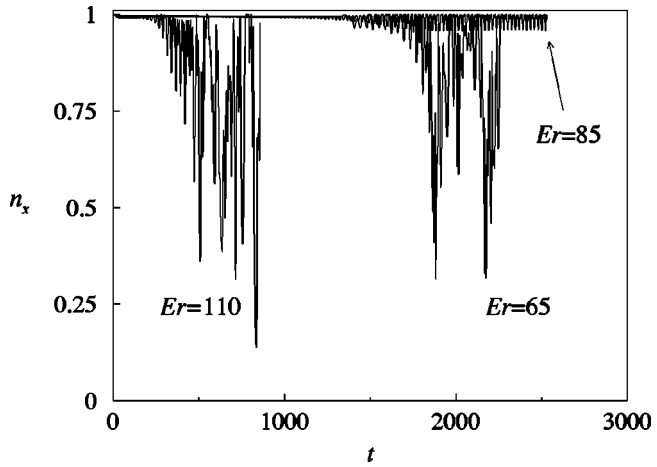

FIG. 8. Small K_3: transitions from an irregular solution at Er = 65 to a regular oscillatory one at Er = 85, and then to another irregular solution at Er = 110.

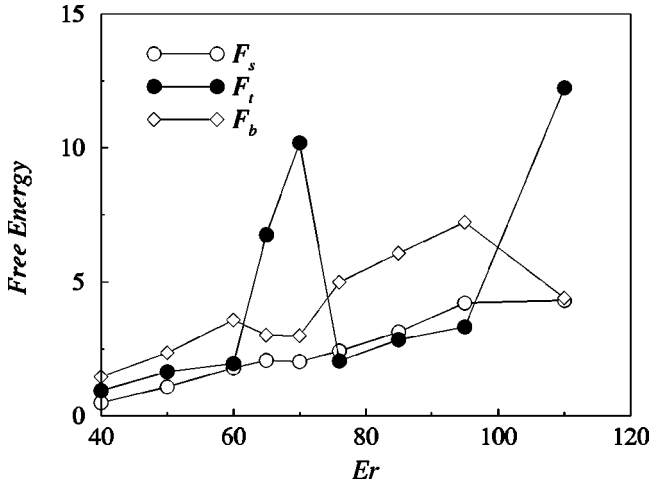

FIG. 9. The two Ericksen cascades as seen from the distortion free energies for $K_3 = 0.5K$, $K_1 = K_2 = K$.

irregular pattern disappears and gives way to a second regular oscillatory regime for Er $> \widetilde{\mathrm{Er}}^o \approx 80$. As Er exceeds $\widetilde{\mathrm{Er}}^i \approx 95$, roll cells once again break up into an irregular pattern with the nucleation of defects. Therefore, there exist two Ericksen number cascades for the small K_3 case. The first comprises four regimes similar to those of the isotropic case, while the second has only the last two regimes. Figure 8 illustrates the higher-Er transitions: from irregular fluctuations at Er = 65 to periodic oscillation at Er = 85, and again to irregular fluctuations at Er = 110. Both irregular regimes produce defects. But the oscillatory regime between them is defect-free, and temporally and spatially periodic. Figure 9 plots the evolution of the free energy for each mode over the two Er cascades. In each cascade, the transition to irregular patterns with defects is accompanied by a sharp increase of the twist energy F_t and a dip in the splay and bend energies. Those are evidently due to the formation of ridges, which cause considerable twist. Similar behavior has been noted in Figs. 2 and 4(a).

Figure 10 compares the Er ranges for the various regimes for four combinations of the elastic constants. As noted before, the onset of roll cells involves mostly bend. As com-

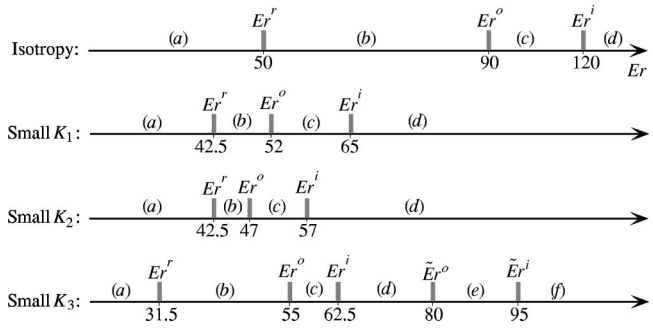

FIG. 10. A summary of the flow-orientational regimes for isotropic and anisotropic elasticity: (a) stable simple shear; (b) steady roll cells; (c) oscillating roll cells; (d) irregular pattern with defects; (e) second oscillatory regime for small K_3; (f) second irregular regime for small K_3.

pared to the isotropic case, therefore, Er^r is greatly reduced for small K_3, but only slightly reduced for small K_1 and K_2. In contrast, the appearance of irregular patterns and defects requires much twist. Hence, Er^i is reduced from 120 to 57 as K_2 decreases from K to $0.1K$. The effects of K_1 and K_3 on Er^i are somewhat weaker. The only mystery in this picture is the second Er cascade that arises for the smaller K_3. Above these finer features, however, Fig. 10 highlights the robustness of the series of instabilities. The sequence from standing wave (steady rolls) to traveling wave (oscillating rolls) and then to chaos (irregular pattern) through breakup or coalescence of microstructures has been observed in many other systems. Examples include inertially and elastically driven Taylor–Couette vortices [Coles 1965; Shaqfeh (1996)], buoyancy-driven boundary-layer flows [Sparrow and Husar (1969)], and interfacial instability in stratified two-phase flows [Sangalli *et al.* (1995)]. Using weakly nonlinear instability theory, Chen *et al.* (1991) and Sangalli *et al.*(1997) have analyzed the last two systems in terms of subharmonic and overtone interactions. Similar mechanisms may be at work in sheared nematics.

D. Anisotropic effects on the conformation of defects

At sufficiently high Er, each of the three cases—small K_1, K_2, or K_3—develops a spatiallly irregular and temporally fluctuating orientation field, out of which ± 1 defect lines nucleate. More careful examination shows that the orientation field and defect configuration possess distinct features for each case. In the following, we will describe these features and attempt to relate them to the different elastic constants. We will take snapshots of the orientation field to illustrate the distinct patterns, but they prevail over the entire space and time.

For small $K_1 = 0.1K$, the director field is marked by long curved ridges, which often have a $+1$ and a -1 defect near their ends. Figure 11(a) illustrates such ridges for $Er = 70$ at $t = 600$ strain units. On either side of the ridge, the director **n** is mostly in the x–y plane, i.e., the plane of the plot. Approaching the ridge, **n** tips out of the page into the primary flow direction z. Thus, a rooftop pattern is formed which, resembling the so-called Néel wall, incurs much splay [Kléman (1988), p. 61]. The nucleation of defects follows the same scenario as described by Feng *et al.* (2001) for isotropic elasticity; a defect pair nucleates on the ridge when local secondary flow splits the rooftop. To explore the role of elastic anisotropy, we have calculated the three modes of distortion and contoured them is Figs. 11(b)–11(d). Indeed, the ridges in (a) correlate closely with the splay distortion in (b). Large twist and bend typically occur near the ends of a ridge or on its sides. Therefore, the prevalent pattern of long curved ridges with defects at the end is a direct result of the reduced K_1. To be more quantitative, the average splay, twist and bend in the rectangular area $7.25 \leqslant x \leqslant 7.45$, $0.2 \leqslant y \leqslant 0.8$ containing a ridge are, respectively, 22.36, 19.78, and 3.40. In comparison, the averages over the entire computational domain are 8.365, 15.49, and 11.53 for the three modes. The prominence of splay at ridges is apparent. Overall, twist is still he greatest distortion, and this will be seen to hold for all three cases of elastic anisotropy [see also Fig. 4(a)]. But for small K_1, the overall percentage of splay (23.6%) is the largest among the three cases.

For small K_2, the director field features localized patches where **n** escapes into the primary flow direction. Figure 12 shows two such areas for $Er = 64$ at $t = 320$ strain units. Pairs of defects may nucleate within the patch, as illustrated by the sketch. The $+1$ defect always assumes a circular pattern and the two remain close together. We have calculated the splay, twist, and bend in the domain, and their contours (not shown here) correlate with the localized patches; each component reaches a maximum in the neighborhood but the exact locations differ. Noting that our orientation pattern extends un-

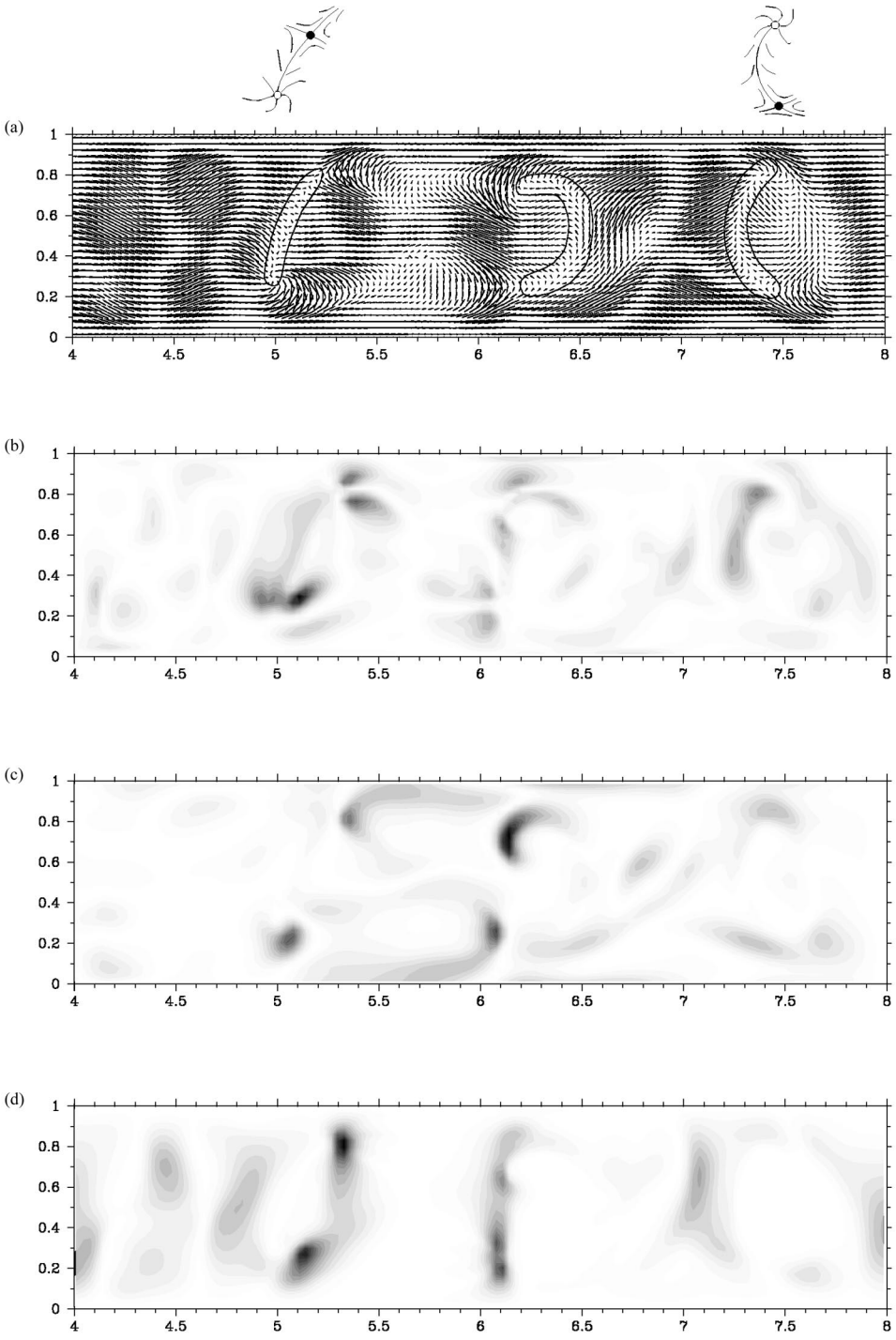

FIG. 11. (a) Director field for $K_1 = 0.1K$, Er $= 70$ at $t = 600$. The loops are drawn to encircle ridges, two of which with defects are illustrated by the sketches. (b) Contours of the splay distortion, $(\nabla \cdot \mathbf{n})^2$. (c) Contours of the twist distortion, $[\mathbf{n} \cdot (\nabla \times \mathbf{n})]^2$. (d) Contours of the bend distortion $|\mathbf{n} \times (\nabla \mathbf{n})|^2$. The contours are scaled by the maximum of each distortion component, and darker areas have larger distortions.

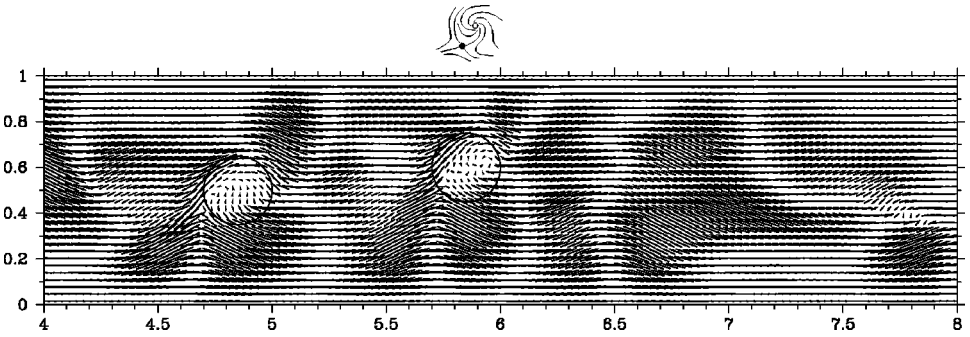

FIG. 12. The director field for Er = 64, $K_2 = 0.1K$ at $t = 320$. The circles indicate localized patches with escaped n, and the sketch illustrates a pair of defects at $x = 5.8$.

changed along the z direction, we expect the circular pattern inside the patch to cause strong twist and moderate bend [Cladis and Kléman (1972); Kléman (1988), p. 52]. This is indeed the case. The amount of splay, twist, and bend averaged in a box enclosing one patch, $5.7 \leqslant x \leqslant 6$, $0.5 \leqslant y \leqslant 0.7$, are 20.03, 114.0, and 35.77, respectively. The averages over the entire domain are 2.351, 15.29, and 7.228. The remarkable dominance of twist at the defect shows that the localized circular patterns are indeed due to the reduced K_2.

For $K_3 = 0.5K$, the director field is characterized by large areas in which **n** escapes to align with the primary flow. Figure 13(a) illustrates such areas for Er = 220. These contrast the elongated ridges for small K_1 and the localized patches for small K_2. Pairs of defects nucleate in such areas and assume orthogonal patterns, the $+1$ defects being radial and the -1 ones being hyperbolic. Note that Er = 220 falls within the second Ericksen cascade for small K_3 (cf. Fig. 10). The irregular regime in the first Er cascade is qualitatively similar with orthogonal defects, albeit in smaller numbers. Based on the two previous cases, one naturally seeks to explain the orthogonal defects in terms of increased bend. The distortion contours show, however, that the defect-laden escaped areas do not correspond to large distortions in any mode. Instead, large splay and bend occur in the strips between such areas, while large twist also appears between these areas and the anchoring walls. Averaged splay, twist, and bend in the escaped area $4.3 \leqslant x \leqslant 5$, $0.2 \leqslant y \leqslant 0.8$ are 3.241, 3.534, and 0.3148, respectively. These are remarkably small in comparison with overall averages of 9.146, 22.74, and 17.47 for the three modes. Thus, the escaped areas contain very weak distortion, and the defects have little impact on the energy budget of the entire material. As a result, one cannot explain the orthogonal defects energetically; they incur very little bend in particular. Since the defects reflect only slight deviations of **n** from z, one may speculate that they have a hydrodynamic rather than elastic origin. A direct correlation between the secondary flow [Fig. 13(e)] and the director field is not apparent, however. Away from the defects, the elastic energy is at work; the overall percentage of bend (35.4%) is the highest among the three anisotropic cases.

The relationship between elastic anisotropy and defect conformation has been studied before in a different context. By fitting experimental micrographs of the **n** field near $\pm 1/2$ defects in thin LCP films, Hudson *et al.* (1993) and Wang *et al.* (1994) determined an apparent elastic anisotropy of the material: $\epsilon = (K_1 - K_3)/(K_1 + K_3)$. Their results showed ϵ, presumably a material constant, to vary appreciably with position as one approaches the defect cores. This demonstrated the failure of the Frank theory to describe

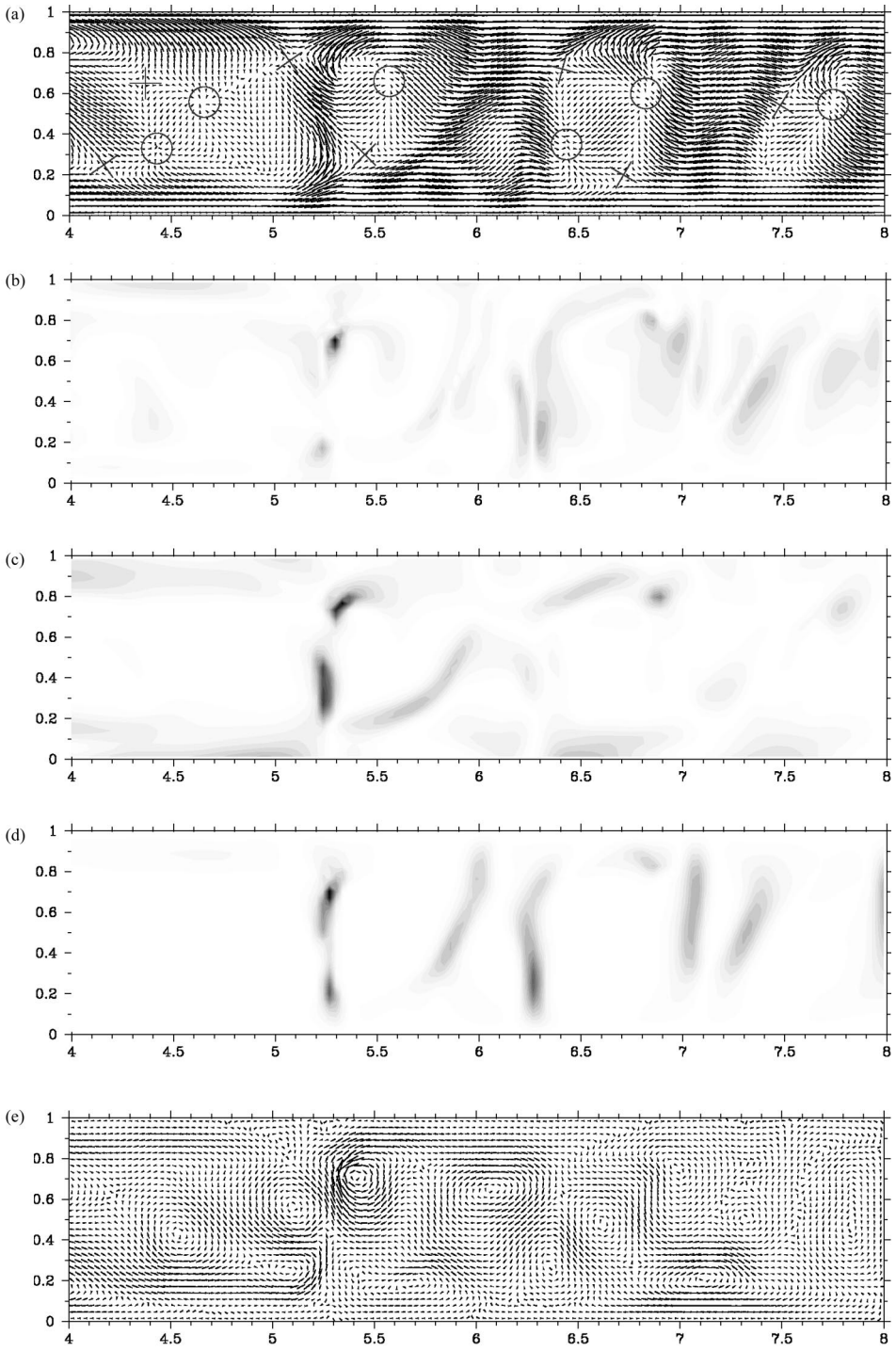

FIG. 13. (a) Director field for $K_3 = 0.5K$, Er $= 220$ at $t = 800$. The crosses and circles indicate the -1 and $+1$ orthogonal defects. Since our plotting software does not shrink the size of arrowheads, the deviation of **n** from z is smaller than might appear. (b),(c),(d) Grayscale contours of splay, twist, and bend. (e) Velocity vector for the secondary flow (u,v).

half-strength defect cores, and the variation of ϵ was explained in terms of molecular rigidity and the different modes of distortion in the core. As regards elastic anisotropy in escaped ± 1 defects, Cladis and Kléman (1972) calculated the stable director fields with isotropic and anisotropic elasticity. Crawford *et al.* (1992) used their solutions to extract K_3/K_1 for real nematics from birefringence patterns. Since none of these studies involves dynamics of flowing nematics, their relevance to our simulations is limited. Our finding that defects of a certain structure incurs particular modes of distortion is consistent with the results of Cladis and Kléman (1972).

E. Relaxation of texture after cessation of shear

After achieving the defect-laden textures discussed in the previous section, we stop the shearing abruptly and examine the relaxation of the textures. In all cases simulated, the relaxation proceeds with ± 1 defects approaching and annihilating each other. This is a well-known scenario from previous experimental observations [Chuang *et al.* (1991); Elias *et al.* (1999)] and numerical simulations [Rey and Tusji (1998)]. Nevertheless, elastic anisotropy manifests itself in distinctive patterns during the relaxation.

As noted earlier, a nematic with a weaker elastic constant tends to sustain greater distortion in the corresponding mode during shearing. In relaxation, on the other hand, that mode will be the least energetically active. Consequently, we expect features representing that mode to persist the longest. For $K_1 = 0.1K$, such a feature is the long curved ridges. The shear is stopped after $t = 600$ strain units of shearing at $\mathrm{Er} = 70$ (cf. Fig. 11), and Fig. 14 illustrates the ensuring relaxation. By $t = 616$, the ridges have contracted [Fig. 14(a)]. The two defects originally on the ridge at $x = 5.1$ have annihilated, and those at the ends of the ridge near $x = 7.4$ are approaching each other [see Fig. 11(a) for original location of ridges and defects]. The flow induced by this relaxation consists of swirls in the x–y plane, which are directly related to the tendency of various areas of the director field to rotate so as to relieve the bend and splay in this plane [Fig. 14(b)]. There is also a w component of the flow, not shown in the plot, due to the relaxation of twist or n_z. The two defects at $x = 7.4$ finally start to annihilate at $t = 660$ [Fig. 14(c)], but the large splay patterns in $5 < x < 6.5$ persist as remnants of the ridges there. These will finally relax after $t = 750$ when the whole domain returns to a single crystal.

For $K_3 = 0.5K$, we stop shearing at $\mathrm{Er} = 220$ after 800 strain units. The ensuing annihilation of defects is more vigorous than the small-K_1 case on account of their larger number and weaker energy (cf. Fig. 13). But the distinguishing feature is the ''director vortices'' formed during the relaxation, which, not surprisingly, involve much bend. Figure 15 illustrates such a pattern at $t = 880$. The vortex pattern persists until $t = 920$ when the pair of defects at $x = 5.5$ annihilate. A nearly uniform director field is achieved at $t = 950$. Note that the core of the $+1$ defect in the director vortex is unusually compact and poorly resolved; **n** shows little escape into the flow direction as it does at the -1 defect. We reduced the grid size by half and still failed to resolve the $+1$ core. Further refinement becomes prohibitively expensive. All other features of the relaxation have been nearly exactly reproduced on the finer mesh, indicating that the poor resolution of the $+1$ core has not compromised the accuracy of the solution elsewhere.

Finally, the relaxation of the small-K_2 solution in Fig. 12 is faster and less eventful. The distortion is mostly restricted to small patches with strong twist. The shear stops at $t = 320$, and the patches have healed completely by $t = 328$. This is much faster than the other two cases even after converting the dimensionless time with respect to Er. (Our dimensionless t is defined in terms of the shear rate V/H. A time scale more appropriate for relaxation should be $\eta H^2/K$, and the corresponding dimensionless t would be the old

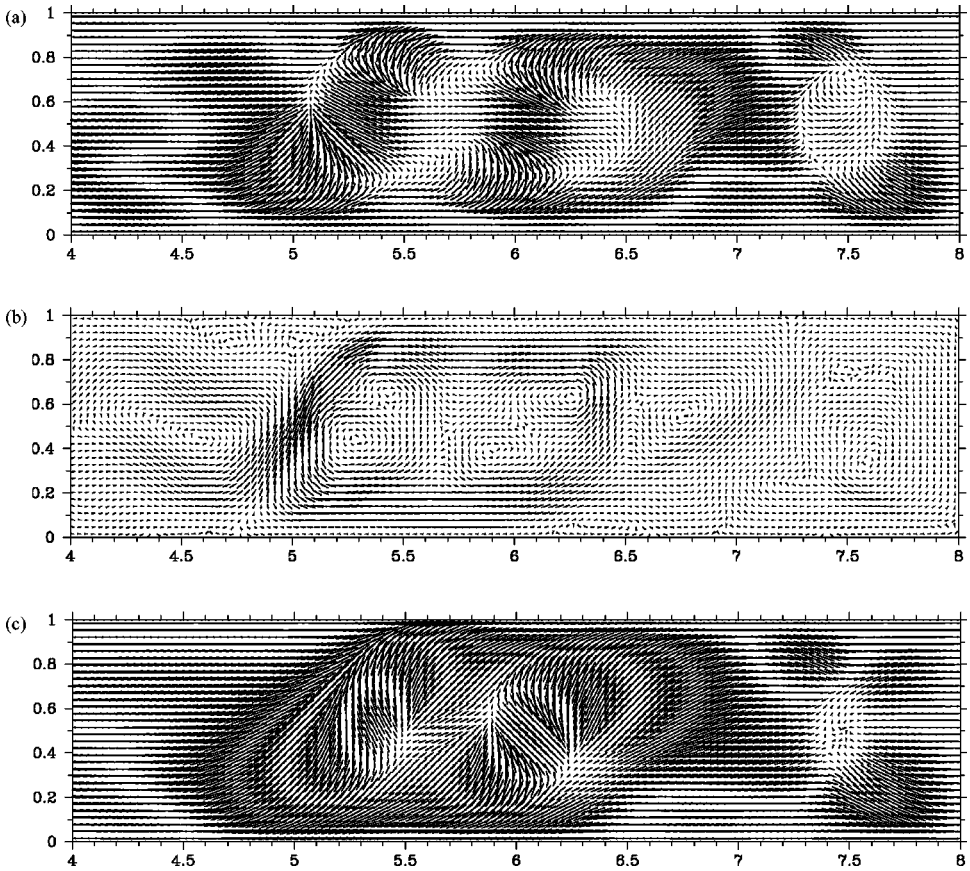

FIG. 14. Relaxation of the shear-induced texture for $K_1 = 0.1K$ and original Er = 70. The shear stops at $t = 600$. (a) Director field at $t = 616$. (b) In-plane velocity field (u,v) at $t = 616$. There is also a w component and the maximum is roughly 0.01 for all three components. (c) Director field at $t = 660$. Note the annihilating pair of defects at $x = 7.5$ and the large splay patterns in $5 < x < 6.5$.

t divided by Er.) This is not surprising since the small-K_2 solution contains fewer defects, and the distortion is weaker and more localized. A distinctive feature is that the relaxation of twist induces a strong velocity component w at the patches. At $t = 324$, for example, the maximum of w is 0.11, about five times the maximum for u and v.

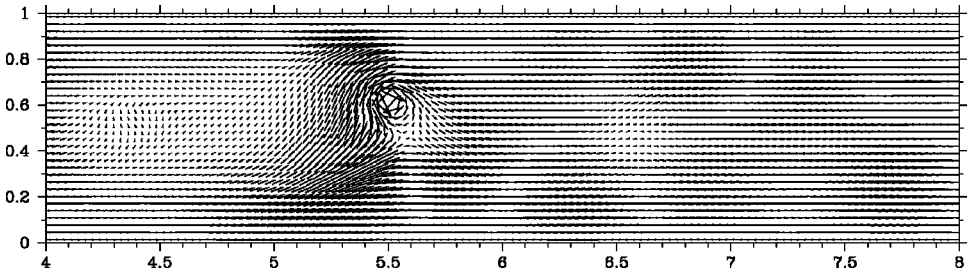

FIG. 15. A ''director vortex'' emerges during relaxation of shear-induced texture at $t = 880$ for $K_3 = 0.5K$ and original Er = 220.

Experimental literature suggests that for small-molecule liquid crystals, textures coarsen and vanish completely in time [Chuang *et al.* (1991)] , whereas for thermotropic liquid crystalline polymers, they approach a stable nonrelaxed state [Elias *et al.* (1999); Colby *et al.* (2001)]. Elias *et al.* (1999) suggested that folding and entanglement of the semiflexible polymer chains may prevent complete relaxation, and likened the stable textured state to a nematic elastomer. Colby *et al.* (2001) argued that a network of defect lines essentially makes the material a viscoelastic solid with a yield stress. Both scenarios are absent in our simulations. The Leslie–Ericksen theory does not incorporate polymer viscoelasticity, let alone reptation of semiflexible chains. Given the simple geometry and our assumption of no-variation along z, the defect lines are all parallel and cannot form a network. The defect density in our simulations is rather too low for entanglement in any event. Thus, our complete relaxation to a single crystal is expected.

IV. CONCLUSIONS

This work explores the role of elastic anisotropy in the flow and orientation of nematic liquid crystals under shear and during subsequent relaxation. Within the parameter ranges covered, we may summarize our numerical results as follows.

(a) The elastic constant K_3, for bend, has the greatest effect in stabilizing a simple shear flow against the onset of roll cells. The elastic constants for splay and twist also tend to suppress roll cells but their effects are much weaker.

(b) With elastic anisotropy, the Ericksen cascade comprises the same regimes as for elastic isotropy: simple shear, steady roll cells, oscillating roll cells, and irregular patterns with defects. But the threshold Ericksen numbers are shifted. A peculiarity is that a weak K_3 may bring about two Ericksen cascades, with regularization and eventual reappearance of the irregular pattern with increasing shear rate.

(c) The defects that nucleate in the irregular regime have features characteristic of the unequal elastic constants. A weaker K_1 or K_2 leads to defect patterns having severe splay or twist, respectively. For the weaker K_3 tested, however, the defects cause only mild distortion and contribute little to the energetics of the system. We surmise that their orthogonal pattern have a hydrodynamic rather than elastic origin.

(d) The shear-induced textures relax completely after the cessation of shear. The mode of distortion corresponding to the weakest elastic constant persists the longest during the relaxation. A weak flow field is induced by the relaxation, which can be related to the tendency of areas of the nematic to rotate so as to relieve the distortion.

The four regimes are a robust feature of the Ericksen cascade, and they are qualitatively the same with or without elastic anisotropy. These have been shown by Feng *et al.* (2001) to agree generally with experimental observations. The effects of elastic anisotropy are either quantitative, as in shifting the critical Ericksen numbers, or reflected by finer details such as the conformation of defects. At present, these effects cannot be verified by experiments. Systematic studies of elastic anisotropy are limited to static defects [e.g., Hudson *et al.* (1993)], and the most comprehensive experiments on sheared nematic polymers so far have not recorded the director field near moving defects. The small-molecule 8CB used by Mather *et al.* (1996b) have $K_1 = K_3 = 2.14K_2$ while the PBG used by Larson and Mead (1993) have $K_1 = 15.5K_2 = 1.59K_3$. Thus, our small-K_2 simulations are probably the most relevant to real nematics.

We close by pointing out the limitations of this work. Disregarding molecular viscoelasticity, the Leslie–Ericksen theory applies to slow flows and mild distortions. Thus, it adequately represents the defects with smooth cores observed in shearing flows of polymeric and small-molecule nematics [Larson and Mead (1993); Mather *et al.*

(1996b)]. In more complex flow geometries, however, $\pm 1/2$ defects do appear and will require a more sophisticated molecular theory [Feng *et al.* (2000)]. Second, our assumption of no-variation along z precludes three-dimensional director turbulence and the formation of a defect network, both prominent features observed or inferred by experiments [Larson and Mead (1993); Colby *et al.* (2001)]. Other important phenomena inaccessible to our simulations include the formation of stripes along the vorticity direction upon the start or cessation of shear [Larson and Mead (1992)] and the development of streamwise patterns in pressure-driven channel flows [Chono *et al.* (1998); Feng and Leal (1999)]. Finally, we have examined three special cases of elastic anisotropy, and can only speculate about more general cases of three unequal K's.

ACKNOWLEDGMENTS

This work was supported in part by a NSF Career Award and a PSC-CUNY Research Award. The authors acknowledge helpful discussions with Professor W. R. Burghardt, Professor H.-C. Chang, Professor R. H. Colby, and Professor R. G. Larson.

References

Burghardt, W. R., and G. G. Fuller, ''Transient shear flow of nematic liquid crystals: manifestations of director tumbling,'' J. Rheol. **34**, 959–992 (1990).

Chen, C. C., A. Labhabi, H.-C. Chang, and R. E. Kelly, ''Spanwise pairing of finite-amplitude longitudinal vortex rolls in inclined free-convection boundary layers,'' J. Fluid Mech. **231**, 73–111 (1991).

Chono, S., T. Tsuji, and M. M. Denn, ''Spatial development of director orientation of tumbling nematic liquid crystals in pressure-driven channel flows,'' J. Non-Newtonian Fluid Mech. **79**, 515–527 (1998).

Chuang, I., N. Turok, and B. Yurke, ''Late-time coarsening dynamics in a nematic liquid crystal,'' Phys. Rev. Lett. **66**, 2472–2476 (1991).

Cladis, P. E., and M. Kléman, ''Non-singular disclinations of strength $S = +1$ in nematics,'' J. Phys. (Paris) **33**, 591–598 (1972).

Colby, R. H., L. M. Nentwich, S. R. Clingman, and C. K. Ober, ''Defect-mediated creep of structured materials,'' Europhys. Lett. **54**, 269–274 (2001).

Coles, D., ''Transition in circular Couette flow,'' J. Fluid Mech. **21**, 385–425 (1965).

Crawford, G. P., J. A. Mitcheltree, E. P. Boyko, W. Fritz, S. Zumer, and J. W. Doane, ''K_{33}/K_{11} determination in nematic liquid crystals: an optical birefringence technique,'' Appl. Phys. Lett. **60**, 3226–3228 (1992).

de Gennes, P. G., and J. Prost, *The Physics of Liquid Crystals*, 2nd ed. (Oxford University Press, Oxford, 1993).

Elias, F., S. M. Clarke, R. Peck, and E. M. Terentjev, ''Equilibrium textures in main-chain liquid crystalline polymers,'' Europhys. Lett. **47**, 442–448 (1999).

Feng, J. J., G. Sgalari, and L. G. Leal, ''A theory for flowing nematic polymer with orientational distortion,'' J. Rheol. **44**, 1085–1101 (2000).

Feng, J., and L. G. Leal, ''Pressure-driven channel flows of a model liquid-crystalline polymer,'' Phys. Fluids **11**, 2821–2835 (1999).

Feng, J. J., J. Tao, and L. G. Leal, ''Roll cells and disclinations in sheared nematic polymers,'' J. Fluid Mech. **449**, 179–200 (2001).

Han, W. H., and A. D. Rey, ''Simulation and validation of nonplanar nematorheology,'' J. Rheol. **38**, 1317–1334 (1994).

Han, W. H., and A. D. Rey, ''Theory and simulation of optical banded textures of nematic polymers during shear flow,'' Macromolecules **28**, 8401–8405 (1995).

Hongladarom, K., W. R. Burghardt, S. G. Baek, S. Cementwala, and J. J. Magda, ''Molecular alignment of polymer liquid crystals in shear flows. 1. Spectrographic birefringence technique, steady-state orientation, and normal stress behavior in poly(benzyl glutamate) solutions,'' Macromolecules **26**, 772–784 (1993).

Hudson, S. D., J. W. Fleming, E. Gholz, and E. L. Thomas, ''Disclination core structure in rigid and semiflexible main-chains polymer nematic liquid crystals,'' Macromolecules **26**, 1270–1276 (1993).

Hudson, S. D., and E. L. Thomas, ''Frank elastic-constant anisotropy measured from transmission-electron-microscope images of disclinations,'' Phys. Rev. Lett. **62**, 1993–1996 (1989).

Kléman, M., *Points, Lines, and Walls in Liquid Crystals, Magnetic Systems and Ordered Media* (Wiley, New York, 1988).

Kupferman, R., M. N. Kawaguchi, and M. M. Denn, ''Emergence of structure in a model of liquid crystalline polymers with elastic coupling,'' J. Non-Newtonian Fluid Mech. **91**, 255–271 (2000).

Larson, R. G., ''Roll-cell instabilities in shearing flows of nematic polymers,'' J. Rheol. **37**, 175–197 (1993).

Larson, R. G., and D. W. Mead, ''Development of orientation and texture during shearing of liquid-crystalline polymers,'' Liq. Cryst. **12**, 751–768 (1992).

Larson, R. G., and D. W. Mead, ''The Ericksen number and Deborah number cascades in sheared polymeric nematics,'' Liq. Cryst. **15**, 151–169 (1993); Corrigendum: **20**, 265 (1996).

Manneville, P., and E. Dubois-Violette, ''Shear flow instability in sheared nematic liquids: Theory steady simple shear flows,'' J. Phys. (Paris) **37**, 285–296 (1976).

Mather, P. T., D. S. Pearson, and R. G. Larson, ''Flow patterns and disclination-density measurements in sheared nematic liquid crystals. I. Flow-aligning 5CB,'' Liq. Cryst. **20**, 527–538 (1996a).

Mather, P. T., D. S. Pearson, and R. G. Larson, ''Flow patterns and disclination-density measurements in sheared nematic liquid crystals. II. Tumbling 8CB,'' Liq. Cryst. **20**, 539–546 (1996b).

Rey, A. D., and M. M. Denn, ''Dynamic phenomena in liquid-crystalline materials,'' Annu. Rev. Fluid Mech. **34**, 233–266 (2002).

Rey, A. D., and T. Tsuji, ''Recent advances in theoretical liquid crystal rheology,'' Macromol. Theory Simul. **7**, 623–639 (1998).

Sangalli, M., C. T. Gallagher, D. T. Leighton, H.-C. Chang, and M. J. McCready, ''Finite amplitude wave evolution at the interface between two viscous fluids: theory and experiments,'' Phys. Rev. Lett. **75**, 77–80 (1995).

Sangalli, M., M. J. McCready, and H.-C. Chang, ''Stabilization mechanisms of short waves in stratified gas-liquid flow,'' Phys. Fluids **9**, 919–939 (1997).

Sgalari, G., L. G. Leal, and J. J. Feng, ''The shear flow behavior of LCPs based on a generalized Doi model with distortional elasticity,'' J. Non-Newtonian Fluid Mech. **102**, 361–382 (2002).

Shaqfeh, E. S. G., ''Fully elastic instabilities in viscometric flows,'' Annu. Rev. Fluid Mech. **28**, 129–185 (1996).

Sparrow, E. M., and R. B. Husar, ''Longitudinal vortices in natural convection flow on inclined surfaces,'' J. Fluid Mech. **37**, 251–255 (1969).

Suen, J. K., Y. L. Joo, and R. C. Armstrong, ''Molecular orientation effects in viscoelasticity,'' Annu. Rev. Fluid Mech. **34**, 417–444 (2002).

Wang, Q., ''A hydrodynamic theory for solutions of nonhomogeneous nematic liquid crystalline polymers of different configurations,'' J. Chem. Phys. **116**, 9120–9136 (2002).

Wang, W., T. Hashimoto, G. Lieser, and G. Wegner, ''Elastic constant anisotropy, core structure of wedge disclinations and optical texture of main-chain P-4-BCMU liquid crystals,'' J. Polym. Sci., Part B: Polym. Phys. **32**, 2171–2186 (1994).